inorganics

MDPI

Article

The Photochemistry of $Fe_2(S_2C_3H_6)(CO)_6(\mu\text{-}CO)$ and Its Oxidized Form, Two Simple [FeFe]-Hydrogenase CO-Inhibited Models. A DFT and TDDFT Investigation

Federica Arrigoni [1], Giuseppe Zampella [1], Luca De Gioia [1], Claudio Greco [2,*] and Luca Bertini [1,*]

[1] Department of Biotechnology and Biosciences, University of Milano-Bicocca, 20126 Milan, Italy; federica.arrigoni@unimib.it (F.A.); giuseppe.zampella@unimib.it (G.Z.); luca.degioia@unimib.it (L.D.G.)
[2] Department of Earth and Environmental Sciences, University of Milano-Bicocca, 20126 Milan, Italy
* Correspondence: claudio.greco@unimib.it (C.G.); luca.bertini@unimib.it (L.B.)

Abstract: Fe^IFe^I $Fe_2(S_2C_3H_6)(CO)_6(\mu\text{-}CO)$ (**^{1}a–CO**) and its Fe^IFe^{II} cationic species (**^{2}a$^+$–CO**) are the simplest model of the CO-inhibited [FeFe] hydrogenase active site, which is known to undergo CO photolysis within a temperature-dependent process whose products and mechanism are still a matter of debate. Using density functional theory (DFT) and time-dependent density functional theory (TDDFT) computations, the ground state and low-lying excited-state potential energy surfaces (PESs) of **^{1}a–CO** and **^{2}a$^+$–CO** have been explored aimed at elucidating the dynamics of the CO photolysis yielding $Fe_2(S_2C_3H_6)(CO)_6$ (**^{1}a**) and $[Fe_2(S_2C_3H_6)(CO)_6]^+$ (**^{2}a$^+$**), two simple models of the catalytic site of the enzyme. Two main results came out from these investigations. First, **a–CO** and **^{2}a$^+$–CO** are both bound with respect to any CO dissociation with the lowest free energy barriers around 10 kcal mol^{-1}, suggesting that at least **^{2}a$^+$–CO** may be synthesized. Second, focusing on the cationic form, we found at least two clear excited-state channels along the PESs of **^{2}a$^+$–CO** that are unbound with respect to equatorial CO dissociation.

Keywords: metal-carbonyl complexes; [FeFe]-hydrogenases; density functional theory; time-dependent DFT; organometallic photochemistry

Citation: Arrigoni, F.; Zampella, G.; De Gioia, L.; Greco, C.; Bertini, L. The Photochemistry of $Fe_2(S_2C_3H_6)(CO)_6(\mu\text{-}CO)$ and Its Oxidized Form, Two Simple [FeFe]-Hydrogenase CO-Inhibited Models. A DFT and TDDFT Investigation. *Inorganics* **2021**, *9*, 16. https://doi.org/10.3390/inorganics9020016

Academic Editor: Duncan Gregory
Received: 5 January 2021
Accepted: 4 February 2021
Published: 9 February 2021

1. Introduction

In recent times, the study of substituted binuclear carbonyl species has gained vast popularity in the context of bioinorganic chemistry due to the fact that the hydrogenase enzymes are currently known for their specificity towards dihydrogen oxidation/evolution invariably include a binuclear carbonyl-containing moiety in their active site [1]. These enzymes, which encompass either only iron ions as metal cofactors ([FeFe]-hydrogenases), or both nickel and iron ([NiFe]-hydrogenases), have inspired the design and synthesis of a plethora of synthetic models to date [2–4], with diiron models being actually prevalent in literature. Such prevalence depends not only on the interest raised by the knowledge that [FeFe]-hydrogenases are extremely efficient [5] but also on the fact that diiron hexacarbonyls of the general formula $Fe_2(SR)_2(CO)_6$—which closely resemble the diiron portion of FeFe-hydrogenase active site, see Figure 1—had been known for seventy years before the publication of the first X-ray structure of the enzyme [6,7]. The availability of a large number of biomimetic catalysts has proved to be the main asset in the quest for a deeper understanding of hydrogenase chemistry [8]. For example, a biomimetic complex described Camara, and Rauchfuss [9] has proved highly valuable to confirm the hypothesis that H_2-binding and splitting in [FeFe]-hydrogenases occur on a single Fe center in the active site (the so-called "distal" iron ion, Fe_d in Figure 1) [10,11]. Interestingly, the same Fe center is thought to be directly involved also in the enzyme inhibition mediated by carbon monoxide [12–14]. CO inhibition is a key topic that has bearings for the perspective [FeFe]-hydrogenases utilization for industrial purposes, as the contact of the enzyme with

even traces of CO, can completely impair hydrogenase activity [15]. Still, many aspects of the chemistry of CO-inhibited [FeFe]-hydrogenases are far from being fully understood. This is true not only for the rather complex photochemistry occurring at the CO-inhibited active site (vide infra) but also with reference to the possibility of structural rearrangements occurring at the active site in concomitance with CO-binding [14,16,17]. Notwithstanding such open issues, biomimetic modeling has had a relatively limited impact so far for the elucidation of the (photo)chemical processes that can occur after CO inhibition, which is mainly due to the small number of biomimetic models of the CO-inhibited enzyme described to date. In any case, the availability of the latter [18] has stimulated positive feedback between experiments and theory, which allowed relating the hardness of ligands in biomimetic models with the stability of key stereoelectronic features in the latter [18,19]. The theory-experiment interplay proved relevant also in more recent studies in which density functional theory (DFT) calculations were used to rationalize the structural outcomes of CO-inhibition and subsequent reduction of the enzyme that gives place to over-saturated forms of the active site [20].

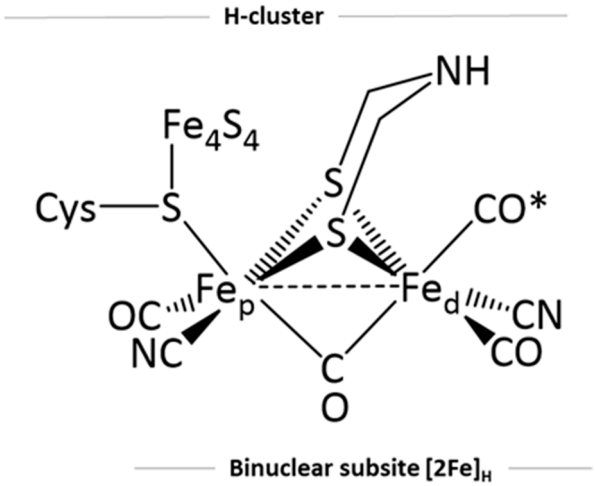

Figure 1. The active site of [FeFe]-hydrogenases, generally referred to as the H-cluster; its diiron portion "$[2Fe]_H$" directly involved in the binding of incipient substrates (H_2 and H^+) and inhibitors is highlighted. The carbonyl ligand marked with an asterisk represents an exogenous CO ligand behaving as an inhibitor. A cysteinyl sulfur bridges the diiron subsite with a $[Fe_4S_4]$ subsite that completes the H-cluster composition. The two Fe atoms of the diiron subsite are labeled with subscripts "d" (distal) or "p" (proximal), depending on their position with respect to the $[Fe_4S_4]$ subsite.

As far as the photochemistry of the CO inhibited form of the enzyme is concerned, it was found to be light-sensitive at cryogenic temperature. CO photolysis is a typical organometallic light-driven process [21], and this type of temperature-dependent mechanism has been already observed in $Fe_2(CO)_9$ photolysis, as pointed out by Chen et al. [22]. In this case, the structure of the $Fe_2(CO)_8$ photoproduct depends on the reaction condition: photolysis up to 35 K yields the $Fe_2(CO)_8$ bridged form, while at the higher temperature, the unbridged form is obtained.

This photolytic process is temperature-dependent and has been studied by EPR [23] and IR spectroscopy [22,24]. At low temperature (6–8 K), the initial axial EPR signal of the CO inhibited form is converted to that of the active form in the absence of CO. This photoproduct arises from the loss of the exogenous CO restoring the initial active form. The illumination at a higher temperature (14–30 K) yields a different photoproduct with a rhombic EPR signal. The IR spectra of this second photoproduct are characterized by the loss of the band associated with the bridging CO. According to the model proposed by Chen et al. [22], the photolyzed ligand can be the bridging one or a terminal one. In this latter case, a successive conversion of the bridging CO to terminal CO would take

place. On the contrary, Rosenboom et al. [24] interpreted their IR spectra for the second photoproduct as the photolysis of two CO ligands (the CO bridging and the exogenous CO).

Among the synthetic models of the $\{Fe_2S_2\}$ subcluster, $Fe_2(S_2C_3H_6)(CO)_6$ (**^{1}a** hereafter) can be considered the simplest one [25]. This complex has been extensively studied, and it is able to electrocatalyze proton reduction, although with a mechanism different compared with that of the enzyme [26,27]. **^{1}a** has one bridging coordination position still available, which may be occupied by a CO ligand.

Fe^IFe^I $Fe_2(S_2C_3H_6)(CO)_6(\mu\text{-}CO)$ (**^{1}a–CO** hereafter) and its Fe^IFe^{II} cation (**^{2}a$^+$–CO** hereafter) have never been synthesized and represent simple biomimetic models for the CO-inhibited $\{Fe_2S_2\}$ subcluster. These have been previously investigated by DFT in a study on the CO affinity of the series of Fe^IFe^I and Fe^IFe^{II} models of the [FeFe]-hydrogenase active site [28]. According to the 18-electron rule, these two models are oversaturated [29,30] complexes compared to the **^{1}a** and **^{2}a$^+$** since at least one Fe atom counts 19 valence electrons. Despite this, their formation enthalpy and free-energy are in qualitative agreement with data obtained from the enzyme. In particular, (i) **^{1}a–CO** formation results endothermic and not spontaneous, in agreement with the fact that Fe^IFe^I CO inhibited form has never been observed; (ii) **^{2}a$^+$–CO** formation is exothermic and spontaneous in qualitative agreement with the values obtained by Thauer et al. [31].

The aim of the present study is to outline a general mechanism for CO photolysis in oversaturated diiron systems related to the CO-inhibited FeFe hydrogenase catalytic site. To do so, we investigated the ground state and excited-state potential energy surface (PES) topologies of simple model systems, namely **^{1}a–CO** and **^{2}a$^+$–CO**, by means of DFT and TDDFT. The main targets of this investigation are (i) to predict the stability of the complex toward CO dissociation and (ii) to shed light on the CO photolysis mechanism considering the hypothetical **^{1}a–CO** and **^{2}a$^+$–CO** photolysis

$$\mathbf{^1a\text{-}CO} \rightarrow \mathbf{^1a} + CO$$

$$\mathbf{^2a^+\text{-}CO} \rightarrow \mathbf{^2a^+} + CO$$

as model photolytic processes. While the photochemistry of **^{1}a** and **^{2}a$^+$** has already been investigated in detail [28,32,33], the case of the oversaturated CO forms has not been studied yet. Previous investigations have shown that the absorption spectrum of **^{1}a** is characterized by an intense band at 355 nm along with a weak shoulder at 400 nm. Both features display an MLCT character that always involves the S atomic orbital, therefore indicating Fe $\rightarrow$ S as prevalent CT. For this, the dynamics of the low-energy excited states are mainly dominated by the Fe-S bond elongation/dissociation that favors the rotation of the partial $Fe(CO)_3$ group [32], while CO photolysis is mostly induced by populating higher-energy states. The question that arises on the basis of this evidence is the following: in the case of an oversaturated model such as **a–CO** and **^{2}a$^+$–CO**, would a fully CO dissociative pathway for low-energy excited states emerge? Indeed, as rightly pointed out by Chen and coworkers [22], there is a close analogy between temperature-dependent CO photolysis processes of $Fe_2(CO)_9$ and of the CO inhibited [FeFe]-hydrogenase catalytic site. DFT/TDDFT investigations of the photochemistry of $Fe_2(CO)_9$ evidence two CO dissociation unbound pathways that evolve towards different $Fe_2(CO)_8$ isomers [34,35]. Although $Fe_2(CO)_8$ and $Fe_2(CO)_9$ may be considered all-CO prototypes of the $\{Fe_2S_2\}$ subcluster in its active and CO-inhibited forms, the electronic and geometric structures of a former couple of species are somewhat different from those of the latter two, as we will show in the following sections, and therefore more complex systems must be considered. Moreover, recent investigations show that UVB light photo-inhibits the enzyme [36,37], whereas it is not the case for visible light, suggesting that a fully dissociative character of the lower excitation emerges only when a complex is oversaturated.

2. Results and Discussion

2.1. Ground States

2.1.1. **a–CO** and ^{2}**a**$^{+}$**–CO** Ground State Properties

^{1}**a–CO** and ^{2}**a**$^{+}$**–CO** are binuclear complexes with a global minimum of C_s symmetry with $^{1}A'$ and $^{2}A'$ ground state molecular terms, respectively. As shown in Figure 2, the terminal CO (*t*-CO) ligands can be distinguished between *trans* or *cis* to the bridging propanedithiolate (μ-pdt) ligand. Each *trans* or *cis* CO group can be further distinguished between *anti* and *syn* with respect to the β carbon of CH_2 group of the μ-pdt. Accordingly, the two Fe atoms are classified as *syn* or *anti*.

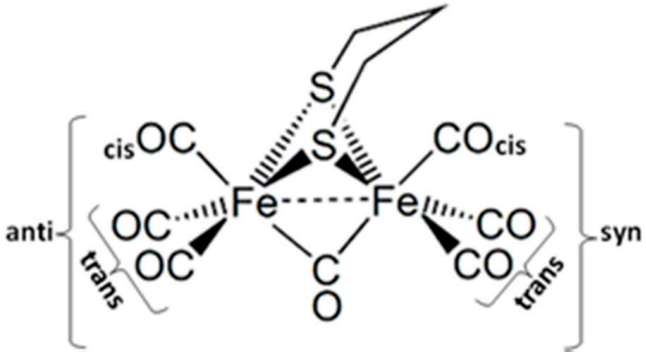

Figure 2. Schematic representation of the $[Fe_2(S_2C_3H_6)(CO)_6(\mu\text{-}CO)]^z$ (z = 0, 1) species analyzed in the present work.

The energy global minimum structures of ^{1}**a–CO** and ^{2}**a**$^{+}$**–CO** are characterized by Fe–Fe bond elongation of 0.452 Å and 0.167 Å, respectively, compared to ^{1}**a** and ^{2}**a**$^{+}$, recalling that this latter has a *syn* rotated C_s minimum geometry [38]. The formation of ^{1}**a–CO** is endothermic and not spontaneous since ^{1}**a** is a saturated complex. On the contrary, ^{2}**a**$^{+}$**–CO** formation is exothermic and spontaneous [38]. Similar considerations regarding the CO-binding process under oxidative conditions have also been reported for more electron-rich diiron models [39–41].

Regarding ^{2}**a**$^{+}$**–CO**, which can be considered as the most promising CO-inhibited model for a successful synthesis, one could ask about the nature of the Fe–Fe bond compared to the ^{2}**a**$^{+}$ parent model. According to the NBO spin population equally distributed on both Fe atoms, the redox state is assigned as $2Fe^{1.5}$. We investigate this issue from the point of view of the quantum theory of atoms in molecules (QTAIM) approach. The topology of ^{1}**a** and ^{2}**a**$^{+}$ electron density are characterized by a Fe–Fe bond critical point (BCP hereafter), which is not found for the corresponding CO oversaturated forms, an evident signal of the weakening of the Fe–Fe bond in the oversaturated moiety. We better characterize this bond by the QTAIM analysis of the electron density using delocalization indexes. The delocalization index δ(A,B) is an integral property that indicates the number of electron pairs delocalized between the two atoms (A and B) and can be considered a covalent bond order [42,43]. In Figure 3, we plotted the δ(Fe,Fe) for the four models considered here plus $Fe_2(CO)_9$ [44], which can be considered as the classic metal carbonyl complex where the nature of the Fe–Fe bond is easily questionable and long debated.

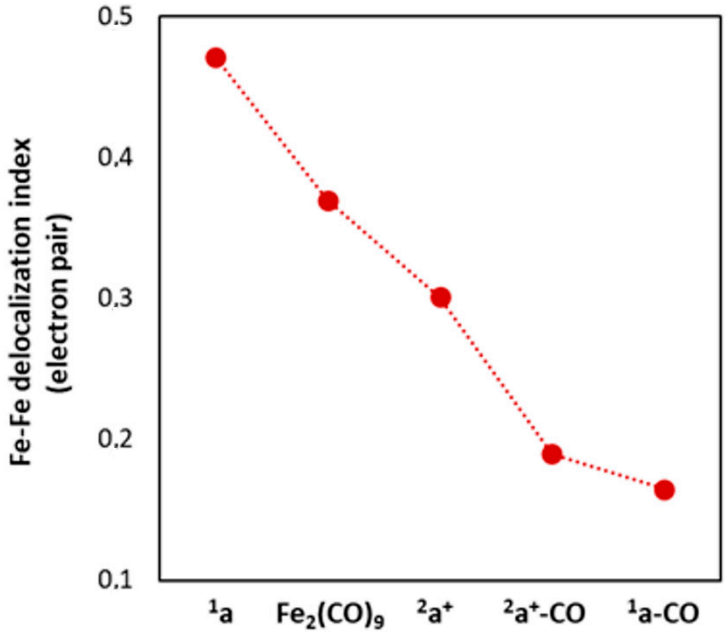

Figure 3. Values of the quantum theory of atoms in molecules (QTAIM) δ(Fe,Fe) delocalization index (in electron pair).

According to the 18-electron counting rule in ^{1}**a** and $Fe_2(CO)_9$, the Fe–Fe bond counts one electron, and this is in line with δ(Fe,Fe) values, both close to 0.5 (0.471 and 0.370, respectively). Going from ^{1}**a** to ^{2}**a**$^+$, the Fe–Fe σ bond highest occupied molecular orbital (HOMO) results singly occupied to the detriment of the Fe–Fe bond, which results weakened according to a δ(Fe,Fe) decreasing of 0.17 electron pair. When a further CO ligand is added to forms ^{1}**a** and ^{2}**a**$^+$, a decrease of δ(Fe,Fe) of 0.306 and 0.111 is observed, respectively, suggesting that the bonding density of the new Fe–C bond comes from the Fe–Fe bond. The value of the δ(Fe,Fe) ^{1}**a**–CO of 0.165 is very low and suggests a very weak or even absent Fe–Fe bond (Figure 3).

2.1.2. ^{1}**a–CO** CO Dissociation Transition States

We investigate three CO dissociation pathways: the dissociation of the *syn cis*, the *syn trans t*-CO and the dissociation of the μ-CO. For each pathway, the corresponding transition state has been characterized.

TS geometry parameters and-free energy barriers are summarized in Figure 4, Figure S1 and in Table 1. The TS structures for the *syn cis* CO dissociation (^{1}**TS1**) retain the C_s symmetry of ^{1}**a–CO** and is characterized by a Fe–C distance of the CO, leaving group equal to 2.618 Å. ^{1}**TS1** further evolves first toward ^{1}**a** *syn* rotated form (which is still a TS) and finally to ^{1}**a**. The structure of the *syn trans* terminal CO ^{1}**TS2** is peculiar. Along the *syn trans* CO dissociation pathway, the μ-CO group has substituted the leaving equatorial CO group, which is partially bound to the CO ligand *cis* to the μ-pdt. ^{1}**TS2** further evolves toward a very intriguing local minimum (^{1}**a–CO(2)**). In this structure, the Fe atoms form two Fe–C bonds with a $(CO)_2$ dimer with O–C–C–O atomic disposition. The Fe–C distances are in the middle between those of a terminal and a bridged CO ligand, and the $Fe(CO)_2$ group is almost planar. Finally, along the μ-CO dissociation pathway, the leaving of the μ-CO is accompanied by a conformational rearrangement of the alkyl chain of μ-pdt (^{1}**TS3**) that brings one of the hydrogen atoms of the bidentate ligand closer to Fe. The Fe_2S_2 tetrahedrane unit becomes almost planar (S–Fe–Fe-S dihedral angle equal to 148.2°), with a Fe–Fe distance increased by 0.519 Å compared to ^{1}**a–CO**.

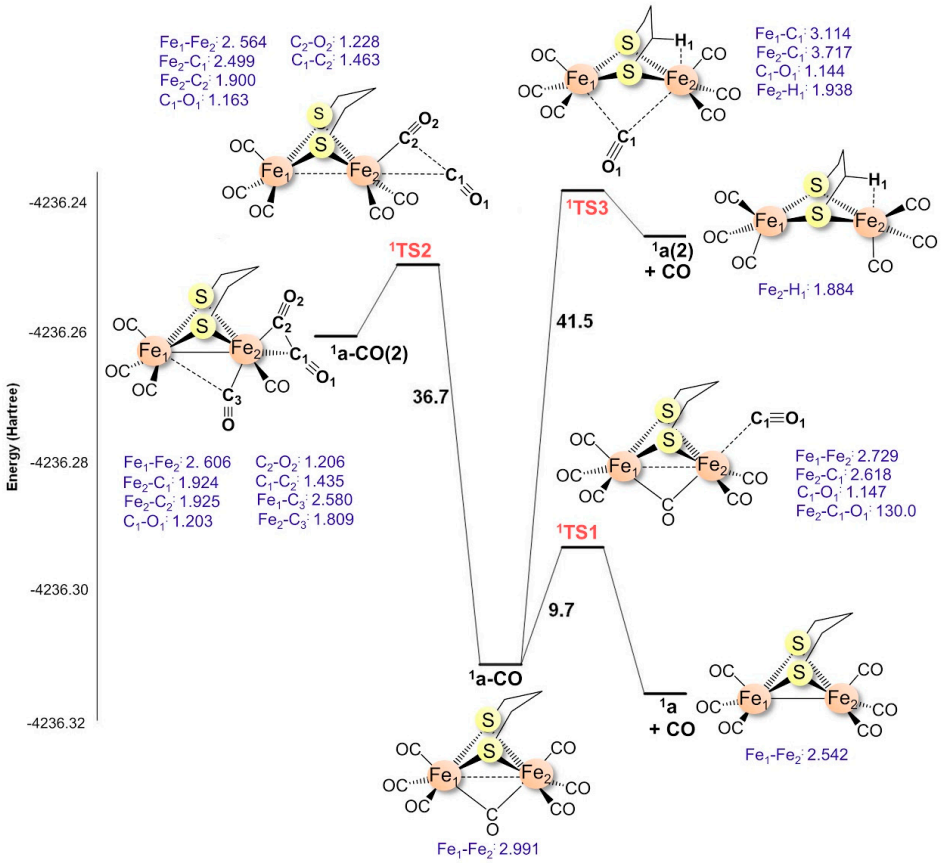

Figure 4. Total density functional theory (DFT) energy diagram and optimized main geometry parameters of **^{1}a–CO** and *cis syn*, *trans syn* and μ-CO CO dissociation transition states and products. The energy in Hartree and free-energy barriers in kcal·mol^{-1}. Distances are in Å and angles in degrees.

Table 1. CO dissociation-free energy barriers (**ΔG ‡**, in kcal·mol^{-1}). Imaginary normal mode (i) frequency (in cm^{-1}). ‡: this is a popular symbol for free energy barriers.

	CO	I	ΔG ‡
^{1}a–CO	*syn cis*	145.5i	9.7
	syn trans	102.3i	36.7
	μ-CO	77.2i	41.5
^{2}a$^+$–CO	*syn cis*	76.4i	14.6
	syn trans	124.8i	53.0
	μ-CO	40.6i	33.5
^{3}a–CO	*syn cis*	111.4i	11.5
	syn trans	99.6i	12.5
	μ-CO	54.1i	8.2

The structure of **^{1}TS3** is also very similar to the TS structure found by Greco et al. [27] relative to the H_2 evolution of the (μ-pdt)$Fe_2(CO)_6H_2$ adduct. **^{1}TS3** further evolves to a local minimum (**^{1}a(2)**) 44.5 kcal·mol^{-1} higher in energy with respect to **^{1}a**. This fact could be explained by considering this isomer as electronically unsaturated in the framework of the 18 electrons rule because of the breaking of the Fe–Fe bond. Finally, the structure of this isomer resembles the rhombus form of $Fe_2S_2(CO)_6$ [45], previously characterized as TS along the tetrahedrane-butterfly isomerization path. According to the free energy barrier, only *syn trans* CO dissociation is a chemically available process.

2.1.3. Transition States for ^{2}**a**$^{+}$**–CO** Dissociation

The TS structures for the *syn cis* CO dissociation (^{2}**TS1**$^{+}$) is similar to that found on the ^{1}**a–CO** PES, but with a Fe–C distance of the leaving group 0.388 Å longer (Figure 5 and Figure S2). At variance with ^{1}**TS3**, this TS evolves toward the *syn* rotated ^{2}**a**$^{+}$ form, which is the global minimum of the ^{2}**a**$^{+}$ PES. The TS for the *syn trans* CO dissociation (^{2}**TS2**$^{+}$) is characterized by the simple elongation of the Fe–C distance to 2.519 Å and the bending of the Fe–C–O angle to 139.3°. At the same time, the μ-CO partially loses its bridging character, moving toward the *syn* Fe atom. ^{2}**TS2**$^{+}$ evolves as ^{2}**TS1**$^{+}$ to ^{2}**a**$^{+}_{\mathbf{syn}}$. The TS for the μ-CO leaving (^{2}**TS3**$^{+}$) is characterized by the simple increasing of the Fe–Cμ distances and the decreasing of the Fe–Fe distance and evolving toward the ^{2}**a**$^{+}$ all terminal ligand. Two further pathways for CO release have been characterized, although energetically impeded. The first (through ^{2}**TS4**$^{+}$) is similar to the one found for ^{1}**a–CO**, which entails the formation of ^{1}**TS2** along the *syn trans* CO dissociation (Figure 4). Here, however, ^{2}**TS4**$^{+}$ evolves towards CO release, giving ^{2}**a**$^{+}$. The other additional pathway implies ^{2}**TS5**$^{+}$, providing a second hypothetical route for μ-CO detachment. In analogy to ^{1}**TS3** (Figure 4), this is accompanied by a conformational rearrangement of the alkyl chain of μ-pdt that brings one of the hydrogen atoms of the bidentate ligand closer to Fe. The Fe–C distances of the leaving μ-CO group and the Fe–Fe distance result to be very elongated. This TS structure further evolves to a high-energy local minimum (^{2}**a**$^{+}$**(2)**).

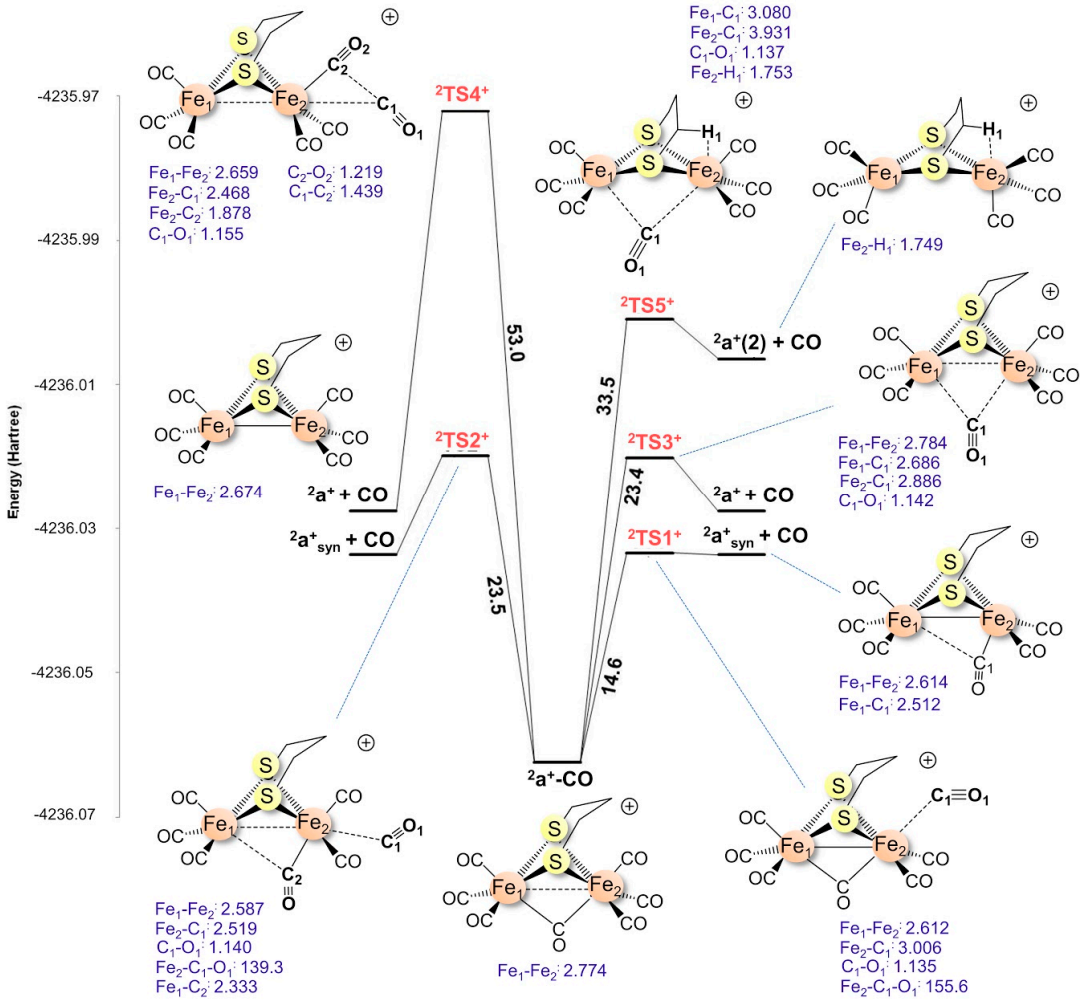

Figure 5. Total DFT energy diagram and optimized main geometry parameters of ^{2}**a**$^{+}$**–CO** and *cis syn*, *trans syn* and μ-CO CO dissociation transition states and products. The energy in Hartree and free-energy barriers in kcal·mol^{-1}. Distances are in Å and angles in degrees.

2.2. Excited States

2.2.1. Electronic Transitions

The simulated spectra of **^{1}a–CO** and **^{2}a^{+}–CO** were computed at the optimized ground state geometry (Table 2), covering a spectral range between 350 and 700 nm (see Figure 6).

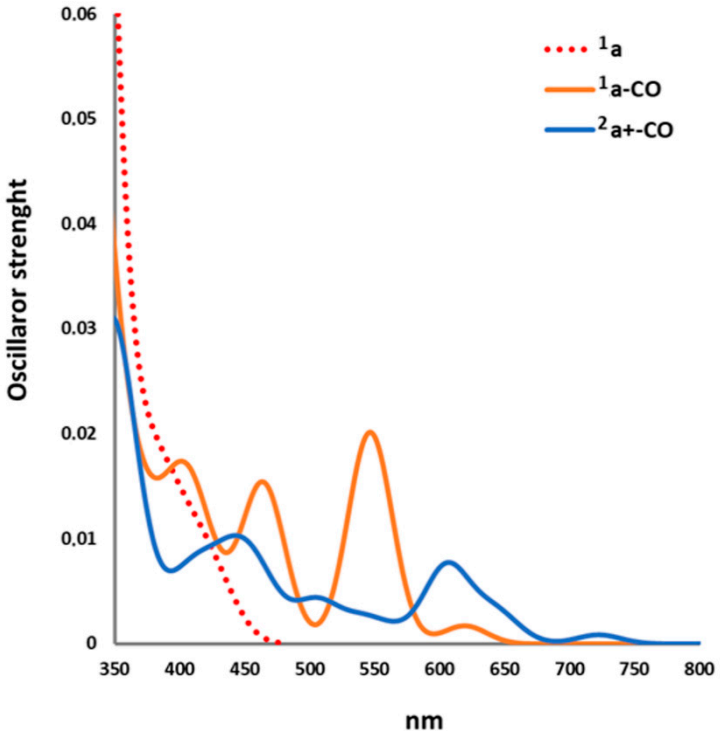

Figure 6. Time-dependent density functional theory (TDDFT) spectra of **^{1}a–CO** and **^{2}a^{+}–CO**. The spectrum computed for **a** (ref. [33]) at the same level of theory is also reported for comparison. Stick spectra were first generated and then convoluted (solid line) using oscillator strength weighted Gaussian distribution functions centered on the computed excitation energies (nm) with halfwidths at half-maxima of 40 nm.

^{1}a–CO singlet electronic excitations are of HOMO(67a′) → LUMO+n (n = 0–9) type. The first two lowest energy transitions involve HOMO(67a′) → LUMO(37a″) and HOMO(67a′) → LUMO+1(38a″) mono-electronic excitations, respectively. In Figure 7 are reported the HOMO, LUMO and LUMO+1 **^{1}a–CO**.

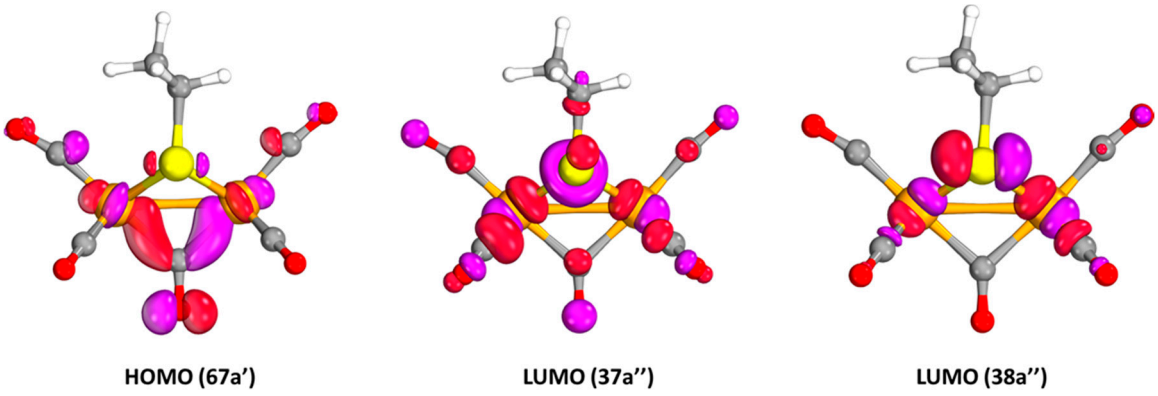

Figure 7. MO isosurfaces (0.05 a.u) for HOMO, LUMO and LUMO+1 of **^{1}a–CO**.

According to the FMO shapes and atomic orbital composition (Figure 7):

(i) HOMO is a sort of three center-two electron Fe–Fe bonding MO through μ-CO; (ii) the lowest unoccupied molecular orbital (LUMO) and LUMO+1 are similar in energy and mainly made of Fe-S and *trans* Fe–C orbitals in antibonding combinations. Therefore, the first two excitations have a Fe → S and Fe → *trans* CO charge transfer (CT) character. On average, LUMO+3 to LUMO+9 are characterized by significant contributions of the *trans* CO orbital contribution, and therefore HOMO → LUMO+n (n = 3–9) are Fe,S → *trans* CO CT bands.

The ^{2}**a^{+}–CO** electronic spectrum is mainly dominated by the SOMO(67a′(α)) → LUMO+n (n = 0.5) and HOMO-n → 67a′(β). In detail, LUMO+4/LUMO+9 are mainly characterized by strong *trans* CO orbital contributions in Fe–C antibonding combinations. The percentage of Mulliken population of the frontier MOs involved in the excitation is reported in Table S1. None of the unoccupied MOs considered is characterized by strong μ-CO orbitals contributions, although all are antibonding or non-bonding with respect to the Fe–C_{μ} bonds. Finally, LUMO+6 and LUMO+7 are also characterized by significant *cis* CO contributions. These results suggest that (i) 9^{2}A″ and 11^{2}A″ states have a strong Fe,S → *trans* CO CT character and therefore could have a repulsive character with respect to the *trans* CO dissociation; (ii) none of the excited states considered presents strong indication of a μ-CO repulsive character according to FMO shape and composition; (iii) 9^{2}A″ state could also be repulsive with respect to *cis* CO dissociation. According to these suggestions, there may be some repulsive excited-state PES along the *trans* or *cis* Fe–C bond elongation, while all excited PESs could be characterized by an energy barrier for the μ-CO dissociation. The scan of the excited-state PESs, presented in the following, has been performed to confirm this picture.

Finally, comparing the spectrum of ^{1}**a–CO** with that of ^{1}**a** computed at the same level of theory, we observe that ^{1}**a** HOMO interacting with the CO LUMO in the classical back-donating scheme rises its energy (see Table S2), placing it in the middle of the ^{1}**a** HOMO-LUMO gap and lowering the wavelength of the MLCT band. From this point of view, CO acts as a chromophore. This fact also implies that ^{1}**a–CO** and ^{2}**a^{+}–CO** excited-state dynamics will be characterized by low-energy μ-CO dissociative channels.

2.2.2. ^{3}**a–CO** Lowest Triplet State

The investigation of the ^{3}**a–CO**, and in particular of the various CO dissociation TSs on such excited-state PES, was performed using ordinary DFT instead of TDDFT since the latter does not allow for the computation of frequency modes.

The lowest triplet state PES has 1^{3}A″ electronic term in C_s symmetry, which results from the excitation *67*a′ → *37*a″. The same minimum structure is also found without any symmetry constraints. According to the shape of the two MOs involved, this excitation can be described as a reorganization of the electron density with a small Fe → S and Fe → *trans* CO CT. By analyzing the natural bond order (NBO) total and spin population, we verified that (i) Fe atoms electron population decreases on average by 0.1 electrons while that of the S atoms increases by 0.074 electrons; (ii) most of the NBO spin population (1.94 electrons) is localized on Fe atoms (0.96 Fe *syn*, 0.36 Fe *anti*), S atoms (0.23 each) and the μ-CO (0.16).

The optimized geometry parameters are reported in Figure 8 and Figure S3. Compared with the singlet ground state (i), the Fe–Fe distance decreases by 0.158 Å; (ii) the μ-CO slightly loses its bridging character (the difference between the shorter and the longer Fe–C distances goes from 0.007 Å (singlet) to 0.281 Å (triplet)); (iii) the *syn* Fe-S distances increase by 0.235 Å. These structural changes are in accordance with the orbital compositions and the characters of the two MOs involved in the monoelectronic excitation. The *67*a′ MO has Fe–Fe antibonding and Fe–C_{μ} bonding character, while the *37*a″ MO composition is mainly made of sulfur and iron orbitals in antibonding combinations. The latter MO also has a *syn trans* Fe–C antibonding character, which accounts for the slight *trans* Fe–C distances increase. It is interesting that no Fe–Fe BCP was found, but the δ(Fe,Fe) value equal to 0.183 is even slightly higher than in ^{1}**a–CO**, thus suggesting that this excitation does not involve the Fe–Fe bond.

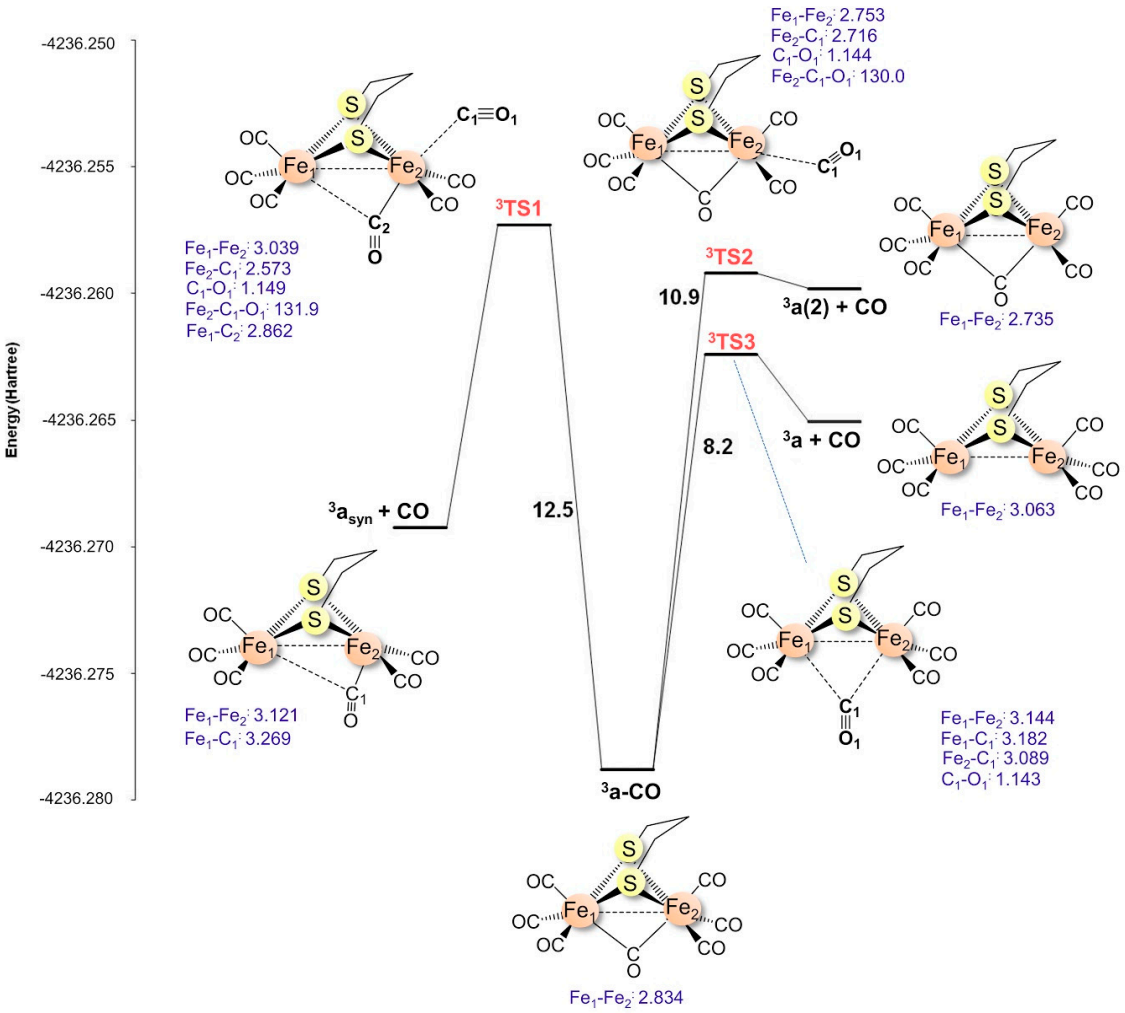

Figure 8. Total DFT energy diagram and optimized main geometry parameters of **^{3}a–CO** and *cis syn*, *trans syn* and μ-CO CO dissociation transition states and products. The energy in Hartree and free-energy barriers in kcal·mol^{-1}. Distances are in Å and angles in degrees.2.2.3 **^{2}a$^+$–CO** 1^2A″ excited-state potential energy surfaces (PES) exploration.

The TS structure along the *syn cis* CO dissociation (**^{3}TS1**) pathway is similar to that found on the ground state PES (Figure 8). The same also holds for the-free energy barrier (only 1.9 kcal·mol^{-1} higher in energy with respect to ground state barrier). This TS evolves to the *syn* rotated form **^{3}a$_{syn}$**, which is also the triplet state PES global minimum. The energy barrier for the *trans* CO and the μ-CO dissociations are predicted to be lower. The TS structure of the *trans* CO dissociation is similar to that found on the cationic **^{2}a$^+$–CO** PES. The TS along the μ-CO dissociation pathway (**^{3}TS3**) structure presents no conformational rearrangement of the alkyl chain of a bidentate group, and the corresponding-free energy barrier is dramatically lowered by 33.3 kcal·mol^{-1} with respect to **^{1}TS3**. **^{3}TS3** evolves to all-terminal triplet **^{3}a**, which is a local minimum of the triplet PES 2.4 kcal·mol^{-1} higher in energy compared to the **^{3}a$_{syn}$** global minimum.

Table 2. Computed excited-state energies, state compositions, and oscillation strengths for **a–CO** and **^{2}a^{+}–CO**. For each transition is reported the molecular term of the corresponding excited state, the excitation energy (in nm), the oscillation strength (f), and the main mono-electronic excitations with the corresponding percentage MO composition. A representation of all relevant MOs involved in electronic transitions can be found in Figure S4.

^{1}a–CO	nm	f	1e	^{2}a^{+}–CO	nm	F	1e
$1^1A''$	767.8	$7{\cdot}10^{-8}$	67a′ → 37a″	$1^2A''$	764.4	$1{\cdot}10^{-5}$	67(α)a′ → 37(α)a″
$2^1A''$	619.1	$2{\cdot}10^{-3}$	67a′ → 38a″	$2^2A''$	722.1	$9{\cdot}10^{-4}$	67(α)a′ → 38(α)a″
$1^1A'$	546.4	0.02	67a′ → 68a′	$1^2A'$	652.4	$1{\cdot}10^{-3}$	66(β)a′ → 67(β)a′ (65%) 65(β)a′ → 67(β)a′ (19%) 67(α)a′ → 68(α)a′ (12%)
$2^1A'$	464.1	$1{\cdot}10^{-2}$	67a′ → 69a′	$2^2A'$	637.7	$2{\cdot}10^{-3}$	65(β)a′ → 67(β)a′ (46%) 66(β)a′ → 67(β)a′ (33%) 67(α)a′ → 68(α)a′(17%)
$3^1A''$	429.9	$6{\cdot}10^{-6}$	67a′ → 39a″	$3^2A''$	608.6	$1{\cdot}10^{-4}$	36(β)a″→ 67(β)a′
$3^1A'$	422.1	$1{\cdot}10^{-3}$	67a′ → 70a′	$3^2A'$	604.9	$7{\cdot}10^{-3}$	67(α)a′ → 68(α)a′ (52%) 65(β)a′ → 67(β)a′ (33%) 63(β)a′ → 67(β)a′ (11%)
$4^1A''$	407.5	$1{\cdot}10^{-3}$	67a′ → 40a″	$4^2A''$	566.2	$9{\cdot}10^{-3}$	35(β)a″ → 67(β)a′
$5^1A''$	405.6	$3{\cdot}10^{-4}$	67a′ → 41a″ (63%) 67a′ → 40a″ (34%)	$4^2A'$	540.1	$2{\cdot}10^{-3}$	64(β)a′ → 67(β)a′
$4^1A'$	403.4	$3{\cdot}10^{-3}$	67a′ → 71a′(69%) 67a′ → 72a′(27%)	$5^2A'$	504.8	$4{\cdot}10^{-3}$	63(β)a′ → 67(β)a′ (63%) 67(α)a′ → 70(α)a′ (17%) 67(α)a′ → 68(α)a′ (14%)
$6^1A''$	400.3	$3{\cdot}10^{-4}$	66a′ → 37a″ (62%) 67a′ → 41a″ (33%)	$5^2A''$	475.6	$2{\cdot}10^{-7}$	34(β)a″ → 67(β)a′(81%) 67(α)a′ → 37(α)a″(16%)
				$6^2A'$	463.4	$4{\cdot}10^{-3}$	67(α)a′ → 69(α)a′
				$6^2A''$	458.9	$2{\cdot}10^{-5}$	67(α)a′ → 39(α)a″ (82%) 34(β)a″ → 67(β)a′ (16%)
				$7^2A'$	442.5	$7{\cdot}10^{-3}$	67(α)a′ → 70(α)a′ (78%) 63(β)a′ → 67(β)a′ (15%)
				$7^2A''$	433.0	$5{\cdot}10^{-7}$	66(α)a′ → 38(α)a″ (42%) 66(β)a′ → 38(β)a″ (27%) 66(β)a′ → 37(β)a″ (14%) 65(β)a′ → 37(β)a″ (5%)
				$8^2A''$	430.3	$3{\cdot}10^{-7}$	65(α)a′ → 37(α)a″ (34%) 65(β)a′ → 37(β)a″ (21%) 65(β)a′ → 38(β)a″ (13%) 66(β)a′ → 38(β)a″ (11%)
				$8^2A'$	412.8	$2{\cdot}10^{-3}$	62(β)a′ → 67(β)a′ (31%) 36(α)a″ → 37(α)a″ (28%) 36(β)a″ → 37(β)a″ (18%) 36(α)a″ → 38(α)a″ (8%)
				$9^2A''$	414.5	$1{\cdot}10^{-3}$	67(α)a′ → 40(α)a″
				$10^2A''$	410.2	$2{\cdot}10^{-3}$	66(α)a′ → 37(α)a″ (33%) 66(β)a′ → 37(β)a″ (21%) 67(α)a′ → 41(α)″ (9%) 66(β)a′ → 38(β)a″ (9%)
				$11^2A''$	409.9	$8{\cdot}10^{-3}$	67(α)a′ → 41(α)a″ (87%) 66(β)a′ → 37(β)a″ (4%)
				$9^2A'$	408.3	$7{\cdot}10^{-4}$	36(α)a″ → 38(α)a″ (33%) 36(β)a″ → 38(β)a″ (31%) 36(α)a″ → 37(α)a″ (15%) 66(β)a′ → 68(β)a′ (5%)
				$10^2A'$	405.1	$1{\cdot}10^{-3}$	62(β)a′ → 67(β)a′ (44%) 36(β)a″ → 37(β)a″ (27%) 36(α)a″ → 37(α)a″ (9%)

2.2.3. ^{2}**a**$^{+}$**–CO** 1^{2}A″ Excited-State PES Exploration

1^{2}A″ state is the lowest doublet excited state of ^{2}**a**$^{+}$**–CO**, characterized by the *67*a′(α) → *37*a″(α) mono-electronic excitation. Analogously to ^{3}**a–CO,** this state has both Fe → S and Fe → CO_{trans} MLCT characters. It is possible to explore the corresponding PES at DFT level by imposing the C_s symmetry and the proper MO occupancy (66a′(2)67α′(α)(0)37α″(α)(1)) in order to constrain the wavefunction to the correct electronic term. Using this approach, one can optimize the structure, providing to maintain the molecular symmetry throughout the optimizations. This last point is clearly a limitation that does not allow us to study the structure of the TS. For these reasons, the results obtained cannot be compared in the same way we did for ^{1}**a–CO** and its lowest triplet state PES but provide insights on the topology of the lowest singlet excited-state PES of ^{2}**a**$^{+}$**–CO**, which is the closest model of the first ^{2}**a**$^{+}$**–CO** excited state.

As for the minimum structure, starting from ^{2}**a**$^{+}$**–CO**, the structure converges to a local minimum (Figure 9). The optimized geometric parameters are similar to those obtained for the ^{3}**a–CO** triplet state minimum structure since the mono-electronic excitation is identical. With respect to the ^{2}**a**$^{+}$**–CO** ground state, the Fe–Fe distance decreases by 0.1 Å and *syn* Fe-S distances are increased by 0.229 Å.

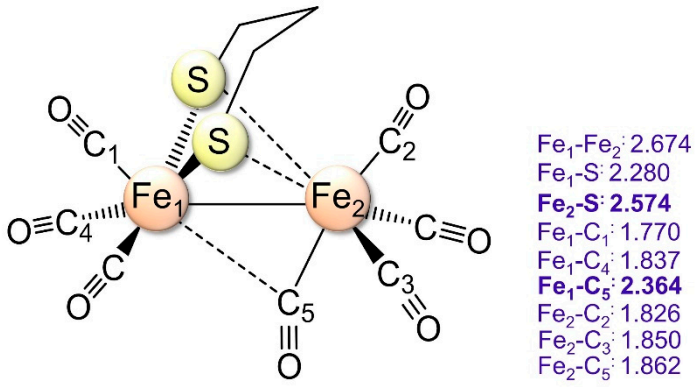

Figure 9. DFT-optimized geometry of the ^{2}**a**$^{+}$**–CO** 1^{2}A″ excited state at DFT level imposing the proper MO occupancy. Distances in Å.

Moreover, we observe a clear loss of the bridging character of the μ-CO, similarly to the case of the μ-H models [46]. The analysis of the NBO atomic and spin populations enlighten the electronic nature of this excited form. Upon excitation is observed (i) a net CT of 0.4 e Fe atoms to *trans* CO ligand induced by the population of the *37*a″(α); (ii) a Fe atomic charges difference of 0.32 e (compared to that of ^{2}**a**$^{+}$**–CO** ground state equal 0.03 e); (iii) a spin localization on distal Fe suggesting a $Fe_d^{II}Fe_p^{I}$ electronic state. This brings to the *trans* Fe–C bonds elongation and, at the same time, determines the Fe–Fe bond shortening. As a side effect, the Fe_d-S is highly elongated.

2.2.4. ^{2}**a**$^{+}$**–CO** Excited States PES Scanning

We considered the scanning of the first 20 excited-states PES along the *syn cis*, *trans cis* and bridged CO dissociation paths starting from the ground state geometry. In Figure 10 are reported the excitation energies along each path for the 20 excited states considered. The scanning along the *syn cis* CO dissociation path does not evidence the dissociative nature of the PESs considered. The scanning along the *syn trans* CO dissociation path evidence at least two dissociative excited-state PESs, as suggested by the complex succession of avoided MO crossing that involves the 7^{2}A″ and 11^{2}A″ states. Similarly, the scanning along the μ-CO dissociation path shows an avoided crossing between 1^{2}A″ and the ^{2}A′ ground state. The other excited PESs are bound with respect to this dissociation.

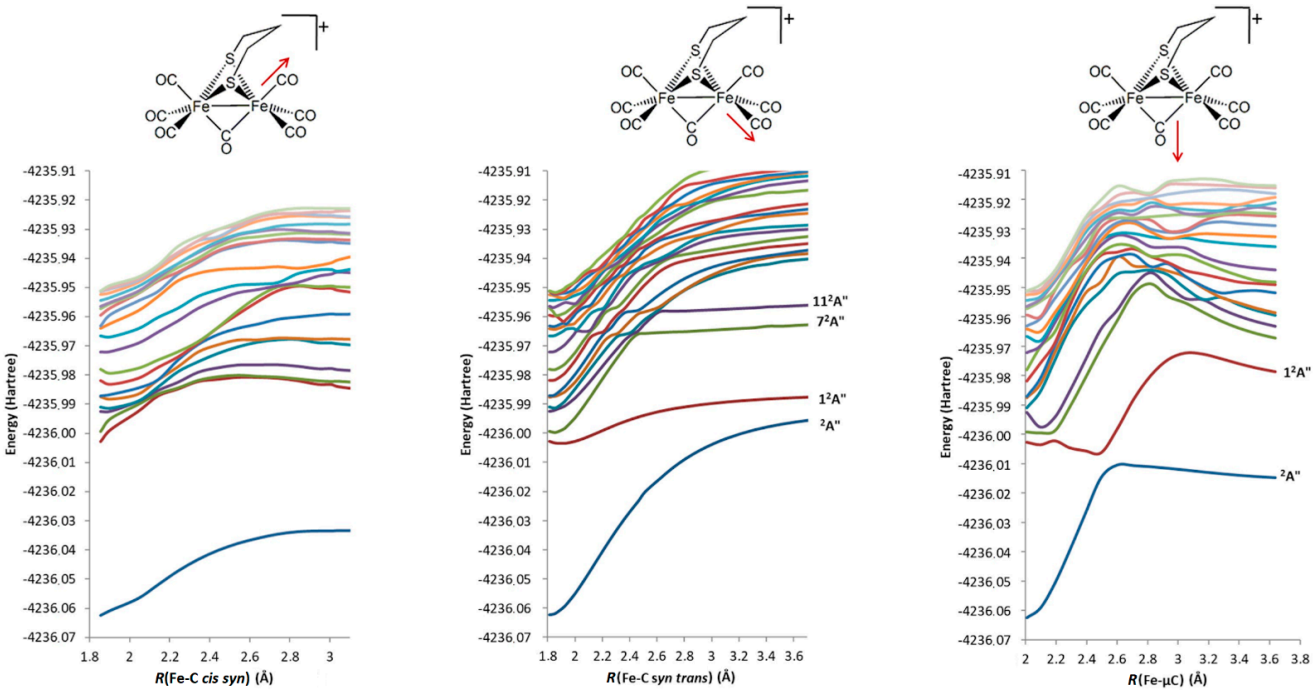

Figure 10. Potential energy surfaces of the ground state and the first 20 singlet excited states of ^{2}**a**$^{+}$**–CO** along the apical and equatorial Fe–CO stretching coordinates (in Å). In *syn trans* and μ Fe–CO plots are also evidenced the excitations whose dynamics lead to the CO photolysis after a series of internal conversions.

As a final step in the investigation of the first ^{2}**a**$^{+}$**–CO** excited state, we optimized its geometry at TDDFT level starting from the 2.2 Å *syn trans* Fe–CO elongated structure identified in the PES scans reported in Figure 10.

TDDFT-optimization energy profile is reported in Figure 11. The optimization does not converge to a stationary point, and the lowest energy structure before the conical intersection is characterized by a *syn trans* Fe–C distance equal to 1.840 Å, in line with the PES scan.

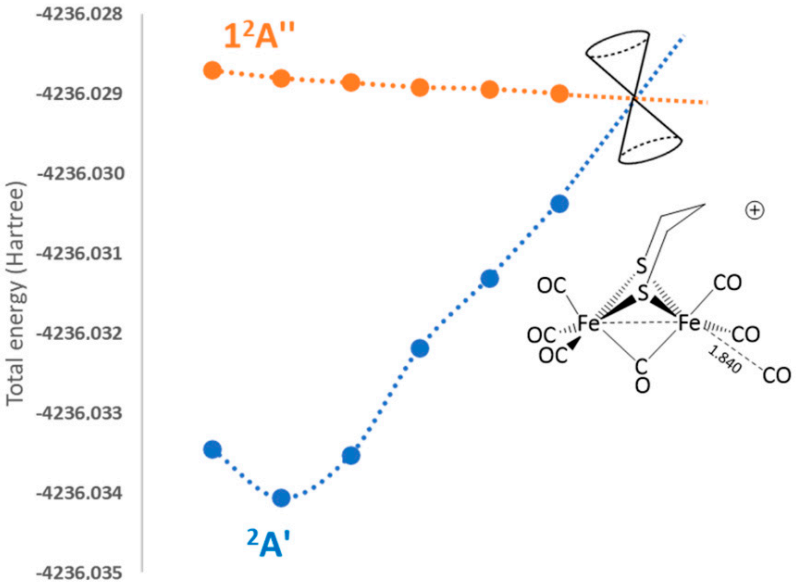

Figure 11. TDDFT-optimization energy profiles for the first excited state of ^{2}**a**$^{+}$**–CO** (1^{2}A″ in orange), starting from the 2.200 Å *syn trans* Fe–CO elongated structure, evidencing the conical intersection with the ground state (in blue) reached after 7 optimization cycles at Fe–CO 1.840 Å. Energies in Hartree.

3. Methods

All computations were carried out using the TURBOMOLE suite of programs [47,48]. The pure gradient generalized approximation (GGA) BP86 [49,50] DFT functional was chosen, in conjunction with a triple-ζ plus polarization split valence quality (TZVP) basis set [51], adopted for all atoms. The resolution-of-identity technique was also adopted [52]. The choice of such a level of theory is justified by its satisfactory performances in the modeling of hydrogenase-related systems [53–56]. The optimization of transition state structures on the ground state PES was carried out according to a procedure based on a pseudo-Newton–Raphson method. All ground state and excited-state geometry optimizations were carried out with convergence criteria fixed 10^{-7} Hartree for the energy and 0.001 Hartree·Å^{-1} for the gradient norm vector. This computational setting provides ground state geometry parameters in concordance with experimental X-ray values and a reasonable picture for excited-state PES properties.

4. Conclusions

The ^{1}**a–CO** and ^{2}**a**$^{+}$**–CO** can be considered as simple models of the [FeFe]-hydrogenase catalytic site in its CO inhibited form. More in general, they are also quite simple models of oversaturated metallo-carbonyl complexes, and the investigation of their photochemistry can be useful to deeply understand the nature of the CO photo-dissociative channels in these moieties.

The ^{1}**a–CO** and ^{2}**a**$^{+}$**–CO** ground state PESs exploration at DFT level evidence that the two complexes are bound with respect to any CO dissociation paths, being the lowest-free energy barriers for the terminal *cis* CO dissociation as large as 9.2 and 14.6 kcal·mol^{-1}, respectively. The other two barriers are much higher and all characterized by a significant distortion of the molecular geometry. The analysis of the electron density at the QTAIM level shows that the stability of the ^{1}**a–CO** and ^{2}**a**$^{+}$**–CO** is possible to the detriment of the Fe−Fe bonds: the bonding density to form the new Fe–C bond comes mainly from the Fe–Fe bond, according to the decrease of the δ(Fe,Fe) going from ^{1}**a** and ^{2}**a**$^{+}$ to ^{1}**a–CO** and ^{2}**a**$^{+}$**–CO**. These results also suggest that at least ^{2}**a**$^{+}$**–CO** could be synthetically achieved.

The investigation of the nature and reactivity of the excited states was carried out in two ways, first at DFT level by imposing spin-triplet state MO occupancy or exploiting the symmetry features of the two models imposing their C_s symmetry; then we performed a PES scan at TDDFT level with no symmetry constraints.

The lowest triplet state of ^{3}**a–CO** is characterized by the HOMO → LUMO monoelectronic excitation, and it is bound with respect to any CO dissociations. The global minimum shows a Fe–Fe bond decreasing and a *syn* Fe-S bond increasing that mirror the features of the LUMO. Since the excitation does not involve Fe–Fe bonding/antibonding MOs, the delocalization index δ(Fe,Fe) is similar to that of ^{1}**a–CO**. The-free energy barriers for *trans syn* and μ-CO dissociation result to be dramatically lowered with respect to those computed for ^{1}**a–CO**. The corresponding TS structures do not show significant geometry distortions. μ-CO dissociation presents the lowest-free energy barrier, and the TS evolves toward the ^{3}**a** all-terminal form, a local minimum on the lowest triplet state PES.

The 1^{2}A″ ^{2}**a**$^{+}$**–CO** PES was explored at the DFT level by imposing the C_s symmetry and the proper MO occupancy. Geometry optimization converges to a local minimum whose structure is similar to ^{3}**a–CO,** but with a larger loss of the bridging character of the μ-CO.

The computations for the excited state at DFT level (^{3}**a–CO** 1^{2}A″ ^{2}**a**$^{+}$**–CO**) strongly suggest that upon excitation, all CO dissociation pathways are photochemically available compared to the ground state, in particular, the *trans syn* and μ-CO ones. This latter conclusion is corroborated by the scan of the ^{2}**a**$^{+}$**–CO** excited PES at the TDDFT level. We observe a clear sequence of internal conversions along the *trans syn* CO (7^{2}A″ and 11^{2}A″ states) and μ-CO dissociation pathways. Moreover, these channels are available upon irradiation in the visible range, populating a Fe,S → CO MLCT band.

A further aspect is related to the differences among ^{1}**a–CO**/^{1}**a** and ^{2}**a**$^+$**–CO**/^{2}**a**$^+$ excited state dynamics. Indeed, the CO inhibited models do not show any photo-isomerization processes as in the case of ^{1}**a** and ^{2}**a**$^+$. This fact suggests a sort of regioselectivity for the CO photolysis of ^{1}**a–CO** and ^{2}**a**$^+$**–CO** in which only *trans* and bridging CO are involved. In conclusion, we can reasonably claim that the low-energy excitations of an oversaturated metallo-carbonyl complex such as those investigated here are characterized by at least one CO dissociative channel, most likely of a terminal ligand. This result can be useful also for a better rationalization of photolysis occurring in the CO inhibited [FeFe]-hydrogenase enzyme. Indeed, it seems reasonable that CO acts as a sort of photoprotector for the H-cluster since it is able to capture visible light when bound to the $[2Fe]_H$ without affecting its functionality. Even when the light in the UV energy range is absorbed, during the excited state dynamics, the system decays through photo-dissociative channels that involve a CO ligand, preventing the irreversible enzyme photo-damage characterized by Sensi et al. [36,37].

Supplementary Materials: The following are available online at https://www.mdpi.com/2304-6740/9/2/16/s1, Figures S1–S3: optimized structures and geometrical parameters of minima and transition states involved in CO dissociation from ^{1}**a–CO**, ^{2}**a**$^+$**–CO**, ^{3}**a–CO**, respectively; Figure S4: relevant ^{1}**a–CO** MOs; Table S1: Mulliken population analysis of ^{2}**a**$^+$**–CO** FMOs; Table S2: MOs eigenvalues for ^{1}**a–CO** and ^{1}**a**; Cartesian coordinates of ^{1}**a–CO**, ^{2}**a**$^+$**–CO**, ^{3}**a–CO**, ^{2}**a**$^+$**–CO** $1^2A''$.

Author Contributions: Conceptualization, L.B.; investigation and formal analysis, F.A., C.G., L.D.G., L.B.; data curation, F.A., L.B., C.G., G.Z.; writing—original draft preparation, L.B., F.A.; writing—review and editing, F.A., L.B., C.G., G.Z., L.D.G. All authors have read and agreed to the published version of the manuscript.

Funding: This research received no external funding.

Institutional Review Board Statement: No applicable.

Informed Consent Statement: No applicable.

Data Availability Statement: Data is contained within the article or supplementary material.

Acknowledgments: The CINECA consortium is gratefully acknowledged for the HPC resources provided in the context of the CINECA-UNIMIB agreement.

Conflicts of Interest: The authors declare no conflict of interest.

References

1. Lubitz, W.; Ogata, H.; Rüdiger, O.; Reijerse, E. Hydrogenases. *Chem. Rev.* **2014**, *114*, 4081–4148. [CrossRef]
2. Kaur-Ghumaan, S.; Stein, M. [NiFe] hydrogenases: How close do structural and functional mimics approach the active site? *Dalton Trans.* **2014**, *43*, 9392–9405. [CrossRef]
3. Kleinhaus, J.T.; Wittkamp, F.; Yadav, S.; Siegmund, D.; Apfel, U.-P. [FeFe]-Hydrogenases: Maturation and reactivity of enzymatic systems and overview of biomimetic models. *Chem. Soc. Rev.* **2020**. [CrossRef]
4. Tard, C.; Pickett, C.J. Structural and Functional Analogues of the Active Sites of the [Fe]-, [NiFe]-, and [FeFe]-Hydrogenases†. *Chem. Rev.* **2009**, *109*, 2245–2274. [CrossRef]
5. Frey, M. Hydrogenases: Hydrogen-activating enzymes. *Chembiochem* **2002**, *3*, 153–160. [CrossRef]
6. Reihlen, H.; Gruhl, A.; v. Hessling, G. Über den photochemischen und oxydativen Abbau von Carbonylen. *Justus Liebig's Ann. Chem.* **1929**, *472*, 268–287. [CrossRef]
7. Peters, J.W.; Lanzilotta, W.N.; Lemon, B.J.; Seefeldt, L.C. X-ray crystal structure of the Fe-only hydrogenase (CpI) from Clostridium pasteurianum to 1.8 angstrom resolution. *Science* **1998**, *282*, 1853–1858. [CrossRef]
8. Arrigoni, F.; Bertini, L.; Breglia, R.; Greco, C.; De Gioia, L.; Zampella, G. Catalytic H_2 evolution/oxidation in [FeFe]-hydrogenase biomimetics: Account from DFT on the interplay of related issues and proposed solutions. *New J. Chem.* **2020**, *44*, 17596–17615. [CrossRef]
9. Camara, J.M.; Rauchfuss, T.B. Combining acid-base, redox and substrate binding functionalities to give a complete model for the [FeFe]-hydrogenase. *Nat. Chem.* **2011**, *4*, 26–30. [CrossRef]
10. Greco, C. H_2 binding and splitting on a new-generation [FeFe]-hydrogenase model featuring a redox-active decamethylferrocenyl phosphine ligand: A theoretical investigation. *Inorg. Chem.* **2013**, *52*, 1901–1908. [CrossRef]
11. Fan, H.J.; Hall, M.B. A capable bridging ligand for Fe-only hydrogenase: Density functional calculations of a low-energy route for heterolytic cleavage and formation of dihydrogen. *J. Am. Chem. Soc.* **2001**, *123*, 3828–3829. [CrossRef] [PubMed]

12. Lacey, A.L.D.; De Lacey, A.L.; Stadler, C.; Cavazza, C.; Claude Hatchikian, E.; Fernandez, V.M. FTIR Characterization of the Active Site of the Fe-hydrogenase fromDesulfovibrio desulfuricans. *J. Am. Chem. Soc.* **2000**, *122*, 11232–11233. [CrossRef]
13. Lemon, B.J.; Peters, J.W. Binding of exogenously added carbon monoxide at the active site of the fe-only hydrogenase (CpI) from *clostridium pasteurianum*. *Biochemistry* **1999**, *38*, 12969–12973. [CrossRef]
14. Greco, C.; Bruschi, M.; Heimdal, J.; Fantucci, P.; De Gioia, L.; Ryde, U. Structural insights into the active-ready form of [FeFe]-hydrogenase and mechanistic details of its inhibition by carbon monoxide. *Inorg. Chem.* **2007**, *46*, 7256–7258. [CrossRef] [PubMed]
15. Bertsch, J.; Müller, V. Bioenergetic constraints for conversion of syngas to biofuels in acetogenic bacteria. *Biotechnol. Biofuels* **2015**, *8*, 210. [CrossRef]
16. Zilberman, S.; Stiefel, E.I.; Cohen, M.H.; Car, R. Resolving the CO/CN ligand arrangement in CO-inactivated [FeFe] hydrogenase by first principles density functional theory calculations. *Inorg. Chem.* **2006**, *45*, 5715–5717. [CrossRef]
17. Duan, J.; Mebs, S.; Laun, K.; Wittkamp, F.; Heberle, J.; Happe, T.; Hofmann, E.; Apfel, U.-P.; Winkler, M.; Senger, M.; et al. Geometry of the Catalytic Active Site in [FeFe]-Hydrogenase Is Determined by Hydrogen Bonding and Proton Transfer. *ACS Catal.* **2019**, *9*, 9140–9149. [CrossRef]
18. Razavet, M.; Borg, S.J.; George, S.J.; Best, S.P.; Fairhurst, S.A.; Pickett, C.J. Transient FTIR spectroelectrochemical and stopped-flow detection of a mixed valence Fe(i)–Fe(ii) bridging carbonyl intermediate with structural elements and spectroscopic characteristics of the di-iron sub-site of all-iron hydrogenase. *Chem. Comm.* **2002**, 700–701. [CrossRef]
19. Greco, C.; Bruschi, M.; Fantucci, P.; De Gioia, L. Relation between coordination geometry and stereoelectronic properties in DFT models of the CO-inhibited [FeFe]-hydrogenase cofactor. *J. Organomet. Chem.* **2009**, *694*, 2846–2853. [CrossRef]
20. Baffert, C.; Bertini, L.; Lautier, T.; Greco, C.; Sybirna, K.; Ezanno, P.; Etienne, E.; Soucaille, P.; Bertrand, P.; Bottin, H.; et al. CO disrupts the reduced H-cluster of FeFe hydrogenase. A combined DFT and protein film voltammetry study. *J. Am. Chem. Soc.* **2011**, *133*, 2096–2099. [CrossRef]
21. Bitterwolf, T.E. Organometallic photochemistry at the end of its first century. *J. Organomet. Chem.* **2004**, *689*, 3939–3952. [CrossRef]
22. Chen, Z.; Lemon, B.J.; Huang, S.; Swartz, D.J.; Peters, J.W.; Bagley, K.A. Infrared Studies of the CO-Inhibited Form of the Fe-Only Hydrogenase from *Clostridium pasteurianum I*: Examination of Its Light Sensitivity at Cryogenic Temperatures†. *Biochemistry* **2002**, *41*, 2036–2043. [CrossRef]
23. Albracht, S.P.J.; Roseboom, W.; Claude Hatchikian, E. The active site of the [FeFe]-hydrogenase from Desulfovibrio desulfuricans. I. Light sensitivity and magnetic hyperfine interactions as observed by electron paramagnetic resonance. *J. Biol. Inorg. Chem.* **2006**, *11*, 88–101. [CrossRef]
24. Roseboom, W.; De Lacey, A.L.; Fernandez, V.M.; Claude Hatchikian, E.; Albracht, S.P.J. The active site of the [FeFe]-hydrogenase from Desulfovibrio desulfuricans. II. Redox properties, light sensitivity and CO-ligand exchange as observed by infrared spectroscopy. *J. Biol. Inorg. Chem.* **2006**, *11*, 102–118. [CrossRef]
25. Darensbourg, M.Y.; Lyon, E.J.; Zhao, X.; Georgakaki, I.P. The organometallic active site of [Fe]hydrogenase: Models and entatic states. *Proc. Natl. Acad. Sci. USA* **2003**, *100*, 3683–3688. [CrossRef]
26. Gloaguen, F.; Rauchfuss, T.B. Small molecule mimics of hydrogenases: Hydrides and redox. *Chem. Soc. Rev.* **2009**, *38*, 100–108. [CrossRef]
27. Greco, C.; Zampella, G.; Bertini, L.; Bruschi, M.; Fantucci, P.; De Gioia, L. Insights into the mechanism of electrocatalytic hydrogen evolution mediated by $Fe_2(S_2C_3H_6)(CO)_6$: The simplest functional model of the Fe-hydrogenase active site. *Inorg. Chem.* **2007**, *46*, 108–116. [CrossRef]
28. Bertini, L.; Greco, C.; De Gioia, L.; Fantucci, P. DFT/TDDFT Exploration of the Potential Energy Surfaces of the Ground State and Excited States of $Fe_2(S_2C_3H_6)(CO)_6$: A Simple Functional Model of the [FeFe] Hydrogenase Active Site. *J. Phys. Chem. A.* **2009**, *113*, 5657–5670. [CrossRef]
29. Tyler, D.R. 19-Electron organometallic adducts. *Acc. Chem. Res.* **1991**, *24*, 325–331. [CrossRef]
30. Astruc, D. Nineteen-electron complexes and their role in organometallic mechanisms. *Chem. Rev.* **1988**, *88*, 1189–1216. [CrossRef]
31. Thauer, R.K.; Käufer, B.; Zähringer, M.; Jungermann, K. The reaction of the iron-sulfur protein hydrogenase with carbon monoxide. *Eur. J. Biochem.* **1974**, *42*, 447–452. [CrossRef]
32. Bertini, L.; Alberto, M.E.; Arrigoni, F.; Vertemara, J.; Fantucci, P.; Bruschi, M.; Zampella, G.; De Gioia, L. On the photochemistry of $Fe_2(edt)(CO)_4(PMe_3)_2$, a [FeFe]-hydrogenase model: A DFT/TDDFT investigation. *Int. J. Quantum Chem.* **2018**, *118*, e25537. [CrossRef]
33. Bertini, L.; Greco, C.; Fantucci, P.; De Gioia, L. TDDFT modeling of the CO-photolysis of $Fe_2(S_2C_3H_6)(CO)_6$, a model of the [FeFe]-hydrogenase catalytic site. *Int. J. Quantum Chem.* **2014**, *114*, 851–861. [CrossRef]
34. Fletcher, S.C.; Poliakoff, M.; Turner, J.J. Structure and reactions of octacarbonyldiiron: An IR spectroscopic study using carbon-13 monoxide, photolysis with plane-polarized light, and matrix isolation. *Inorg. Chem.* **1986**, *25*, 3597–3604. [CrossRef]
35. Bertini, L.; Bruschi, M.; De Gioia, L.; Fantucci, P. Structure and energetics of $Fe_2(CO)_8$ singlet and triplet electronic states. *J. Phys. Chem. A* **2007**, *111*, 12152–12162. [CrossRef] [PubMed]
36. Sensi, M.; Baffert, C.; Greco, C.; Caserta, G.; Gauquelin, C.; Saujet, L.; Fontecave, M.; Roy, S.; Artero, V.; Soucaille, P.; et al. Reactivity of the Excited States of the H-Cluster of FeFe Hydrogenases. *J. Am. Chem. Soc.* **2016**, *138*, 13612–13618. [CrossRef]
37. Sensi, M.; Baffert, C.; Fradale, L.; Gauquelin, C.; Soucaille, P.; Meynial-Salles, I.; Bottin, H.; de Gioia, L.; Bruschi, M.; Fourmond, V.; et al. Photoinhibition of FeFe Hydrogenase. *ACS Catal.* **2017**, *7*, 7378–7387. [CrossRef]

38. Bertini, L.; Greco, C.; Bruschi, M.; Fantucci, P.; De Gioia, L. CO Affinity and Bonding Properties of [FeFe] Hydrogenase Active Site Models. A DFT Study. *Organometallics* **2010**, *29*, 2013–2025. [CrossRef]
39. Arrigoni, F.; Mohamed Bouh, S.; De Gioia, L.; Elleouet, C.; Pétillon, F.Y.; Schollhammer, P.; Zampella, G. Influence of the Dithiolate Bridge on the Oxidative Processes of Diiron Models Related to the Active Site of [FeFe] Hydrogenases. *Chem. Eur. J.* **2017**, *23*, 4364–4372. [CrossRef]
40. Arrigoni, F.; Bouh, S.M.; Elleouet, C.; Pétillon, F.Y.; Schollhammer, P.; De Gioia, L.; Zampella, G. Electrochemical and Theoretical Investigations of the Oxidatively Induced Reactivity of the Complex $[Fe_2(CO)_4(\kappa^2\text{-dmpe})(\mu\text{-adtBn})]$ Related to the Active Site of [FeFe] Hydrogenases. *Chem. Eur. J.* **2018**, *24*, 15036–15051. [CrossRef]
41. Chouffai, D.; Zampella, G.; Capon, J.-F.; De Gioia, L.; Le Goff, A.; Pétillon, F.Y.; Schollhammer, P.; Talarmin, J. Electrochemical and Theoretical Studies of the Impact of the Chelating Ligand on the Reactivity of $[Fe_2(CO)_4(\kappa^2\text{-LL})(\mu\text{-pdt})]$ Complexes with Different Substrates (LL = IMe-CH_2-IMe, dppe; IMe = 1-Methylimidazol-2-ylidene). *Organometallics* **2012**, *31*, 1082–1091. [CrossRef]
42. Macchi, P. Chemical bonding in transition metal carbonyl clusters: Complementary analysis of theoretical and experimental electron densities. *Coord. Chem. Rev.* **2003**, *238–239*, 383–412. [CrossRef]
43. Gatti, C.; Lasi, D. Source function description of metal-metal bonding in d-block organometallic compounds. *Faraday Discuss.* **2007**, *135*, 55–78. [CrossRef] [PubMed]
44. Bertini, L.; Greco, C.; De Gioia, L.; Fantucci, P. Time-dependent density functional theory study of $Fe_2(CO)_9$ low-lying electronic excited states. *J. Phys. Chem. A* **2006**, *110*, 12900–12907. [CrossRef]
45. Bertini, L.; Fantucci, P.; De Gioia, L. On the Photochemistry of the Low-Lying Excited State of $Fe_2(CO)_6S_2$. A DFT and QTAIM Investigation. *Organometallics* **2011**, *30*, 487–498. [CrossRef]
46. Bertini, L.; Fantucci, P.; De Gioia, L.; Zampella, G. Excited state properties of diiron dithiolate hydrides: Implications in the unsensitized photocatalysis of H_2 evolution. *Inorg. Chem.* **2013**, *52*, 9826–9841. [CrossRef]
47. Balasubramani, S.G.; Chen, G.P.; Coriani, S.; Diedenhofen, M.; Frank, M.S.; Franzke, Y.J.; Furche, F.; Grotjahn, R.; Harding, M.E.; Hättig, C.; et al. TURBOMOLE: Modular program suite for ab initio quantum-chemical and condensed-matter simulations. *J. Chem. Phys.* **2020**, *152*, 184107. [CrossRef] [PubMed]
48. Ahlrichs, R.; Bär, M.; Häser, M.; Horn, H.; Kölmel, C. Electronic structure calculations on workstation computers: The program system turbomole. *Chem. Phys. Lett.* **1989**, *162*, 165–169. [CrossRef]
49. Becke, A.D. Density-functional exchange-energy approximation with correct asymptotic behavior. *Phys. Rev. A Gen. Phys.* **1988**, *38*, 3098–3100. [CrossRef] [PubMed]
50. Perdew, J.P. Density-functional approximation for the correlation energy of the inhomogeneous electron gas. *Phys. Rev. B Condens. Matter* **1986**, *33*, 8822–8824. [CrossRef]
51. Schäfer, A.; Huber, C.; Ahlrichs, R. Fully optimized contracted Gaussian basis sets of triple zeta valence quality for atoms Li to Kr. *J.Chem. Phys.* **1994**, *100*, 5829–5835. [CrossRef]
52. Eichkorn, K.; Weigend, F.; Treutler, O.; Ahlrichs, R. Optimized accurate auxiliary basis sets for RI-MP2 and RI-CC2 calculations for the atoms Rb to Rn. *Theor. Chem. Acc.* **1997**, *97*, 119–124. [CrossRef]
53. Goy, R.; Bertini, L.; Rudolph, T.; Lin, S.; Schulz, M.; Zampella, G.; Dietzek, B.; Schacher, F.H.; De Gioia, L.; Sakai, K.; et al. Photocatalytic Hydrogen Evolution Driven by [FeFe] Hydrogenase Models Tethered to Fluorene and Silafluorene Sensitizers. *Chem. Eur. J.* **2017**, *23*, 334–345. [CrossRef] [PubMed]
54. Arrigoni, F.; Rizza, F.; Vertemara, J.; Breglia, R.; Greco, C.; Bertini, L.; Zampella, G.; De Gioia, L. Rational Design of Fe_2 $(\mu\text{-}PR_2)(L)_6$ Coordination Compounds Featuring Tailored Potential Inversion. *Chemphyschem* **2020**, *21*, 2279–2292. [CrossRef]
55. Greco, C.; Fantucci, P.; De Gioia, L.; Suarez-Bertoa, R.; Bruschi, M.; Talarmin, J.; Schollhammer, P. Electrocatalytic dihydrogen evolution mechanism of $[Fe_2(CO)_4(\kappa^2\text{-}Ph_2PCH_2CH_2PPh_2)(\mu\text{-}S(CH_2)_3S)]$ and related models of the [FeFe]-hydrogenases active site: A DFT investigation. *Dalton Trans.* **2010**, *39*, 7320. [CrossRef] [PubMed]
56. Sicolo, S.; Bruschi, M.; Bertini, L.; Zampella, G.; Filippi, G.; Arrigoni, F.; De Gioia, L.; Greco, C. Towards biomimetic models of the reduced [FeFe]-hydrogenase that preserve the key structural features of the enzyme active site; a DFT investigation. *Int. J. Hydrog. Energy* **2014**, *39*, 18565–18573. [CrossRef]